Available online at www.sciencedirect.com

ScienceDirect

Advances in Space Research 62 (2018) 1146–1164

ADVANCES IN SPACE RESEARCH (a COSPAR publication)

www.elsevier.com/locate/asr

3D radar wavefield migration of comet interiors

Paul Sava [a,*], Erik Asphaug [b]

[a] Center for Wave Phenomena, Colorado School of Mines, 1500 Illinois Street, Golden, CO 80401, USA
[b] Lunar and Planetary Laboratory, University of Arizona, 1629 E University Blvd, Tucson, AZ 85721, USA

Received 25 April 2018; received in revised form 6 June 2018; accepted 6 June 2018
Available online 19 June 2018

Abstract

Imaging the interior structure of small planetary bodies facilitates a deep understanding of their origin and evolution, thus addressing fundamental questions about the formation of the Solar System. We show that high resolution 3D imaging of their interior structure is possible using radar waves that reflect from internal discontinuities of dielectric properties. A radar imaging mission at a comet nucleus would have the benefit of orbiting all around a finite and transparent body, collecting echoes that derive only from the target, and processing them collectively in phase.

As is the case in the medical field, imaging a comet nucleus requires its illumination from multiple directions, which can be accomplished with a spacecraft in slow polar orbit around the studied object. Long acquisition time leads to a dense acquisition array resembling that of conventional synthetic aperture radar systems, but completely surrounding the nucleus (4π steradians). Acquisition with an orbiter at large distance from the comet nucleus ($5\times$ the mean diameter) results in relatively coarse data sampling relative to the radar wavelength, thus enabling 3D imaging with a short (< 90 days) mission.

Radar migration is performed using techniques adapted from terrestrial exploration seismology. Wavefield migration identifies interior reflectors by time reversal of monostatic radar data redatumed to the known comet surface for computational speed-up. This technique is applicable to nuclei of arbitrary shape and interior complexity, and it is complementary to wavefield tomography tasked with constraining physical properties in-between the interior interfaces. Migration resolution is identical in all directions (range and cross-range) and it is equivalent to the range resolution of the radar system. Least-squares migration enhances resolution further by deconvolution of the radar wavelet from the reflectivity image.
© 2018 COSPAR. Published by Elsevier Ltd. All rights reserved.

Keywords: Comet; Radar; Wavefield; Imaging; Migration

1. Introduction

This is the second of two articles describing the use of wavefield-based data processing to image the interior of a small planetary body, using high frequency (3–30 MHz) radar reflections acquired from a single orbiting spacecraft (Sava and Asphaug, 2018). This concept is the basis for a proposed mission named **Comet Radar Explorer** to a Jupiter-Family Comet (JFC) (Asphaug et al., 2010). Electromagnetic energy propagates readily through a cold comet nucleus with a transparent, low-scattering dielectric interior (Ciarletti et al., 2017). Radar waves reflect strongly from the back surface of the comet nucleus, taking many different paths in the interior of an irregularly-shaped comet. Therefore, as discussed in detail by Sava and Asphaug (2018), a monostatic reflection experiment is equivalent to innumerable two-way transmission experiments illuminating a comet interior in many diverse directions. This combination of factors provides an ideal opportunity to image in unprecedented detail the three-dimensional interior structure of a comet nucleus using radar waves.

* Corresponding author.
E-mail address: psava@mines.edu (P. Sava).

https://doi.org/10.1016/j.asr.2018.06.009
0273-1177/© 2018 COSPAR. Published by Elsevier Ltd. All rights reserved.

As emphasized in the Planetary Science Decadal Survey, comets are fundamental objects to study and explore because of the decisive role they play in modeling planet and satellite formation and evolution. Inside their broken, eroded, dust- and ice-mantled exteriors they have a deep record that we can barely see via surface expressions imaged by missions like Deep Impact and Stardust NExT (Belton et al., 2007; Veverka et al., 2013) or Rosetta (Sierks et al., 2015; El-Maarry et al., 2015). Whether Solar System formation was quiescent as predicted by most interpretations of the Rosetta observations (Capria et al., 2017), or was dynamically violent in its early evolution as predicted by the Nice model (Morbidelli and Rickman, 2015) and other theories (Batygin et al., 2016), remains an open question. We can only guess whether the kinds of structures expressed at surfaces and in the topography of cometary nuclei, for example in observations of comet 9P/Tempel 1 shown in Fig. 1, extend into their deep interiors (Belton et al., 2007). It might be that the features observed at comet nuclei surfaces are the result of superficial activity in the upper tens of meters and do not reflect accurately their deep interior structure. Clarity on such questions can only come from high resolution 3D imaging of comet interiors.

For reasons described by Safaeinili et al. (2002) and Sava and Asphaug (2018), cometary nuclei are especially well suited to exploration using radar sounders of the sort that have flown to the Moon and Mars and will soon fly to Europa. Orbital radar systems have been spectacularly effective at revealing the detailed vertical structure of the Martian polar layered deposits (Foss et al., 2017). The use of radar sounding at cometary nuclei was proven by the CONSERT experiment onboard Rosetta (Kofman et al., 2015), which beamed a 90 MHz signal through the nucleus in a bi-static geometry, from the orbiter to the ill-fated lander Philae during its descent to the surface of comet 67P/Churyumov-Gerasimenko (67P/C-G).



Fig. 1. Comet 9P/Tempel 1 (Thomas et al., 2013) as it was imaged by the Deep Impact projectile before it struck the nucleus on July 4, 2005. The area closest to the impact is the highest resolution. The nucleus is 5 × 8 km diameter. NASA/JPL/UMD.

The CONSERT radar experiment conducted successfully through almost 2 km of comet material probed its composition and showed it to be low-scattering with little attenuation (Ciarletti et al., 2017), as expected for an extremely cold (perhaps 40 K) porous volatile-rich object. For radar frequencies on the order of 3–30 MHz, scattering losses are even lower. We consider these longer 10–100 m wavelengths because data collection can be made precisely in phase. The combined navigation position and comet shape uncertainty are less than about one meter, and thus echoes from beginning to end of mission can be treated as a single self-consistent experiment.

Of course, not every comet may be like 67P/C-G in internal composition, but even for porous chondrite materials the concept studied here should apply to bodies of kilometer size (Heggy et al., 2012). The lowest risk, highest science value mission would be a rendezvous with any active Jupiter-Family Comet, the family-class of the bilobate Rosetta target 67P/C-G.

The key advantage of a radar reflection imaging mission at a small body is that all reflection data are signal. All observations are radar echoes from structural/compositional contrasts inside or at the surface of the nucleus, plus galactic noise. A-priori knowledge of the comet exterior shape, and in-phase collection of the data, allows all radar echoes to be relocated to their reflection points (the goal of migration), and therefore there is no data "clutter" to be suppressed. Radar imaging of a comet nucleus is global, and therefore an intrinsically 3D problem. Wavefield-based imaging has been developed over the past decades precisely to solve this class of problems. Modern computer power is well-suited to processing radar data rigorously as described in Sava and Asphaug (2018) for tomography, and here for migration.

In the following, we discuss the main elements of wavefield migration, with particular emphasis on high-resolution imaging. We analyze data sampling in the context of orbital radar acquisition, and advocate for imaging methodology with the capacity to maximize spatial resolution for a given radar bandwidth. We illustrate these techniques with a realistic numeric experiment based on a complex comet shape and interior distribution of physical properties.

2. Acquisition geometry

We address the problem of imaging the interior of comet nuclei with radar waves transmitted and recorded by a nadir-pointing orbiting radar, Fig. 2(a). Nuclei are assumed to be spinning around an axis defining their polar directions, and the spacecraft is assumed to be moving

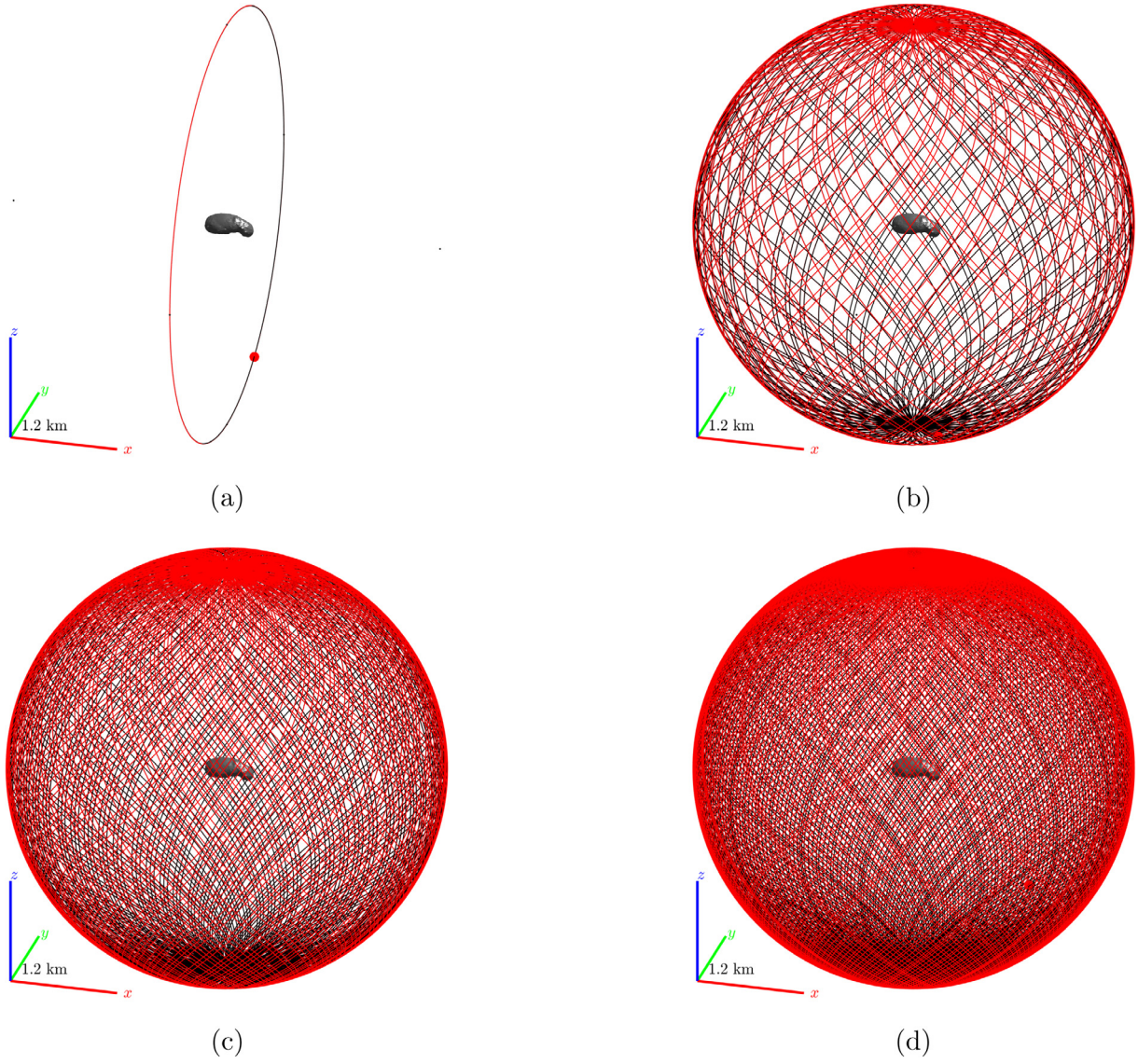


Fig. 2. (a) Spacecraft trajectory represented in a space reference frame and in a comet reference frame for (b) 30, (c) 60, and (d) 90 days. In comet-centric coordinates, the orbiter appears to follow a helical trajectory relative to the comet, and observation points progressively cover the entire orbital sphere.

slowly in a polar orbit (Safaeinili et al., 2002), Fig. 2(a). Seen in a comet reference frame, the spacecraft follows a helical trajectory and can thus observe the nucleus from many independent directions, Fig. 2(b)–(d).

The nucleus illumination with radar waves depends on the acquisition duration. For carefully selected rotation periods of the comet and of the spacecraft, the orbits mapped to comet-centric coordinates do not repeat as a function of acquisition (slow) time, thus increasing the illumination diversity of the comet. Fig. 2(b)–(d) depict progressively higher orbital density for increasing acquisition durations of 30, 60 and 90 days, respectively. Although the spacecraft orbital speed is constant, the comet-centric coverage is not uniform as a function of space. Polar regions have denser coverage than equatorial regions, primarily because the comet tangential velocity is significantly greater at the equator than at higher latitudes. The practical consequence of this configuration is that the observations points are distributed irregularly on a sphere corresponding to the spacecraft orbiter altitude. Moreover, the effective distances between observation points change as a function of acquisition time, as later orbits interleave with earlier ones. These considerations impact data sampling specifications.

3. Wavefield imaging

The wavefield imaging methodology used in this paper derives from techniques developed in the context of exploration seismology (Berkhout, 1982; Clærbout, 1985), and global seismology (Dahlen and Tromp, 1998; Nolet, 2008). Variations of these techniques can also be applied to Ground-Penetrating Radar (Reynolds, 1997; Jol, 2008; Miller and Bradford, 2010), or to Synthetic Aperture

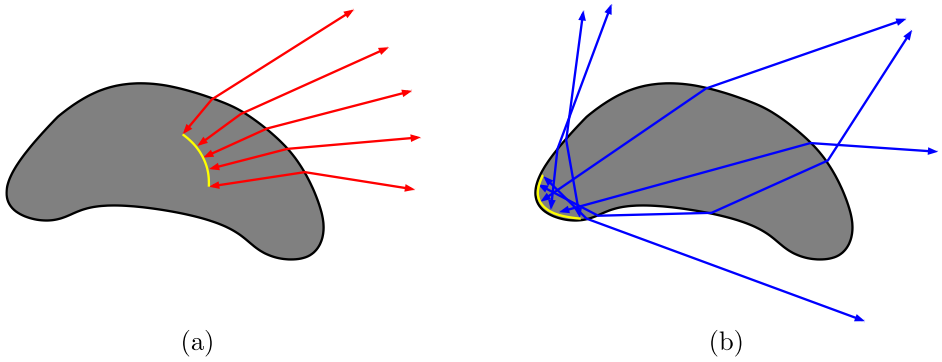


Fig. 3. (a) Schematic representation of a reflection experiment. The **migration** objective is to correctly position reflectors (yellow line) inside the comet nucleus. (b) Schematic representation of a transmission experiment. The **tomography** objective is to infer the physical properties throughout the comet nucleus by enforcing the condition that the back-side reflectors are imaged on the known nucleus shape. (For interpretation of the references to color in this figure legend, the reader is referred to the web version of this article.)

Radar (Rocca et al., 1989; Prati et al., 1990; Cafforio et al., 1991; Sava et al., 2015; Foss et al., 2017; Sava and Asphaug, 2018).

Two wavefield imaging methods are applicable to monostatic radar data:

- Wavefield migration, Fig. 3(a), designed to position interfaces representing dielectric properties contrasts in the comet interior. Migration needs information about the propagation speed inside the comet for correct imaging of reflectors.
- Wavefield tomography, Fig. 3(b), designed to evaluate the wave propagation speed in the comet interior. Tomography needs information about known reflectors to constrain the material properties in the comet interior.

Tomography and imaging are complementary to one-another. Both techniques can handle comets with complex shapes, as well as arbitrary interior geometry and physical properties. In this paper we focus on wavefield migration; wavefield tomography is covered in detail in Sava and Asphaug (2018).

Migration and tomography applied to monostatic data rely on the **exploding reflector model** (Clærbout, 1985). The key idea behind the exploding reflector model is that waves propagating between the radar transmitter antenna and reflectors in the comet interior or the exterior surface return to the radar receiver antenna, co-located with the transmitter, if they reflect at 90° on every interface. If this is the case, the propagation path from the transmitter to the reflector is identical with the path from the reflector to the receiver. Therefore, two-way monostatic reflection data can be treated as if they were one-way data

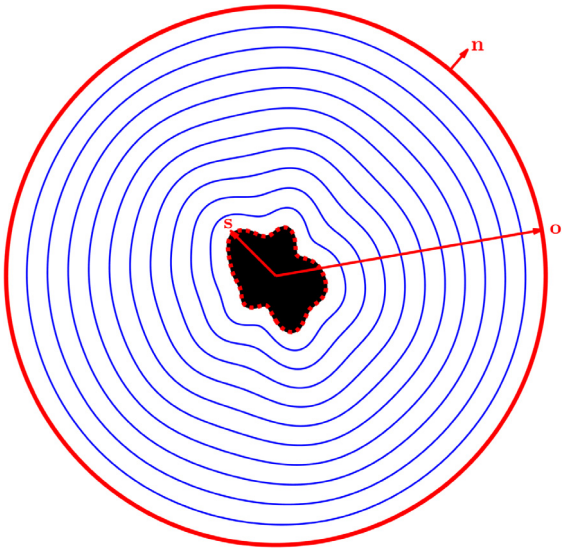


Fig. 4. Schematic representation of wavefield datuming. Radar reflections in orbit (solid red line) are remapped to the surface of the nucleus (dashed red line) using wavefield datuming (blue lines). (For interpretation of the references to color in this figure legend, the reader is referred to the web version of this article.)

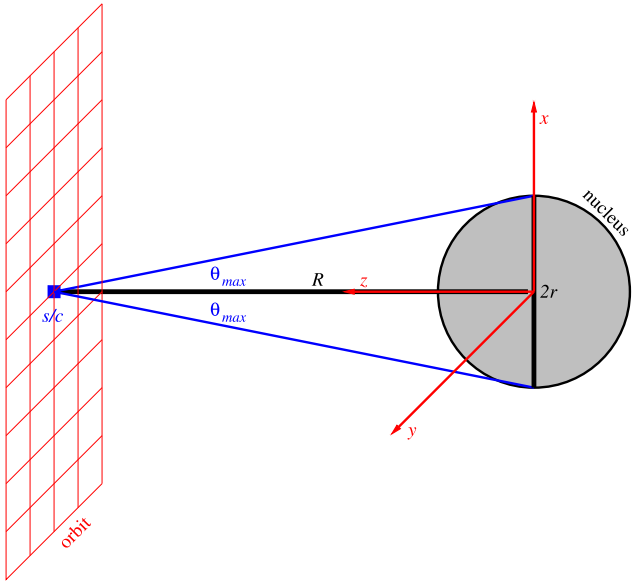


Fig. 5. Geometry defining the maximum aperture angle θ_{max} for an orbiter at radius R from the center of mass of a comet whose mean cross-section is $2r$ as seen from the spacecraft.

representing waves simultaneously triggered on all interior reflectors at the same initial time. Identifying reflectors in the interior of the comet simply amounts to locating the position of the one-way radar waves at their initial time, which can be accomplished via time reversal (Fink et al., 2002).

In practice, two-way monostatic reflection data can be transformed into one-way monostatic data by a sequence of steps: (1) deconvolve the known radar wavelet from the two-way data, (2) reduce in half the propagation time of the deconvolved data, and (3) convolve the radar wavelet back to form one-way data of equivalent bandwidth with the original two-way data.

The main benefit of the exploding reflector model is that it effectively reduces the imaging computational cost, by treating all data as a single experiment. Moreover, this concept does not pose restrictions on waves propagating in complex models with large dielectric contrasts separated by interfaces of arbitrary shapes and orientations, as discussed by Sava and Asphaug (2018).

We assume that acquisition is conducted from a spacecraft at a relatively large distance from the nucleus in order to maintain its orbital stability (Scheeres et al., 1998). As discussed later, this placement has benefits for data sampling, but it also has the drawback that waves propagate for a long duration in free space.

Similar to the technique described and used by Sava and Asphaug (2018), we redatum the radar observations from orbit to the surface of the nucleus, Fig. 4. This process is highly efficient, since it is done in free space with constant velocity, and thus can exploit analytic Green's functions (Aki and Richards, 2002). Datuming relates every orbit location **o** to every surface location **s**, using the normal to the acquisition surface **n** as a guide to limit illumination according to the radar antenna pattern. Following redatuming, the radar waves can be propagated in the comet

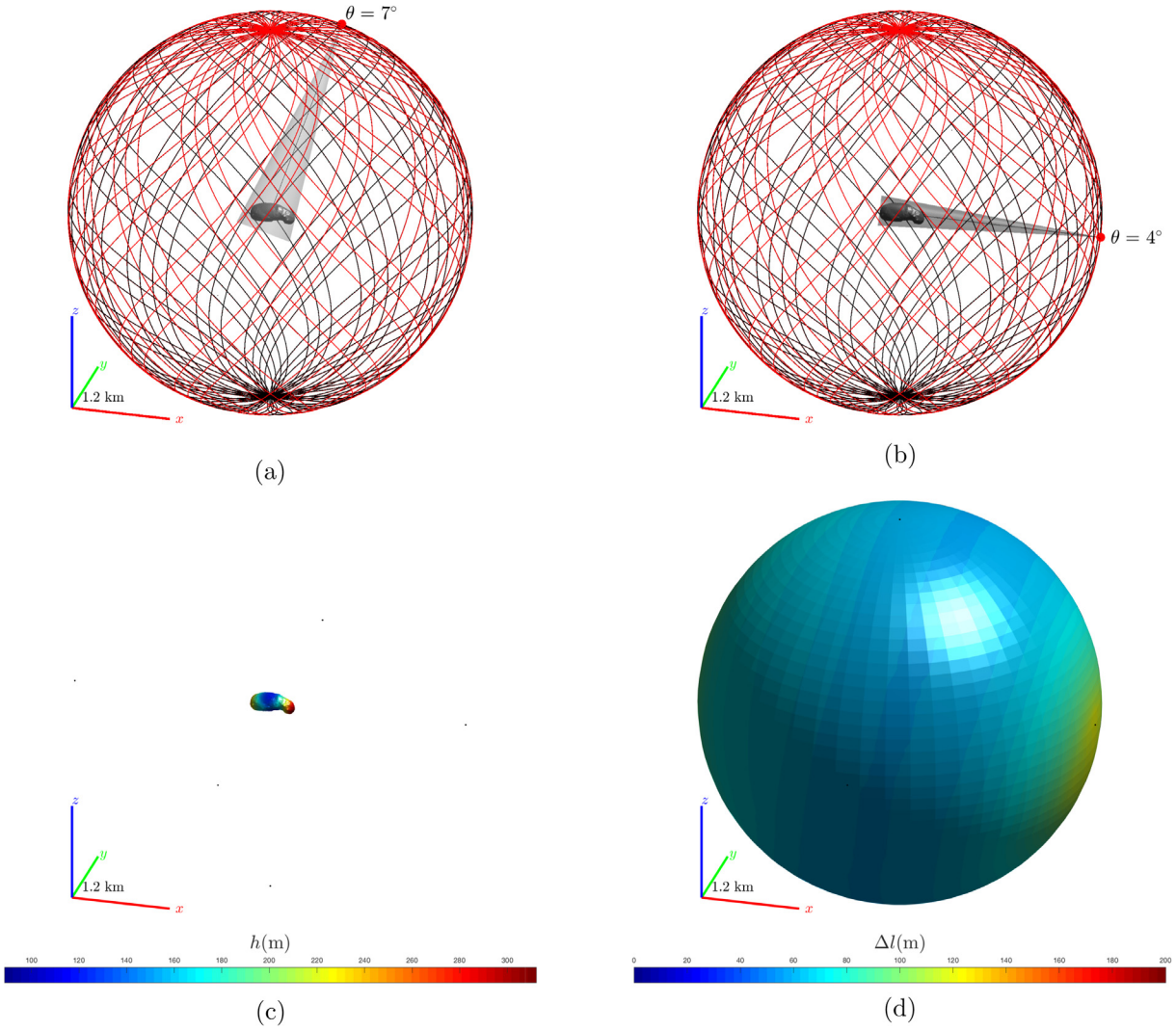


Fig. 6. (a)–(b) Aperture angles θ_{max} from various spacecraft positions in orbit around an irregular comet nucleus. Only waves propagating along directions inside the represented cones give information about the nucleus internal structure. (c) Nucleus topography relative to its center of mass, and (d) sampling distance as a function of orbital position – inversely proportional to the comet size.

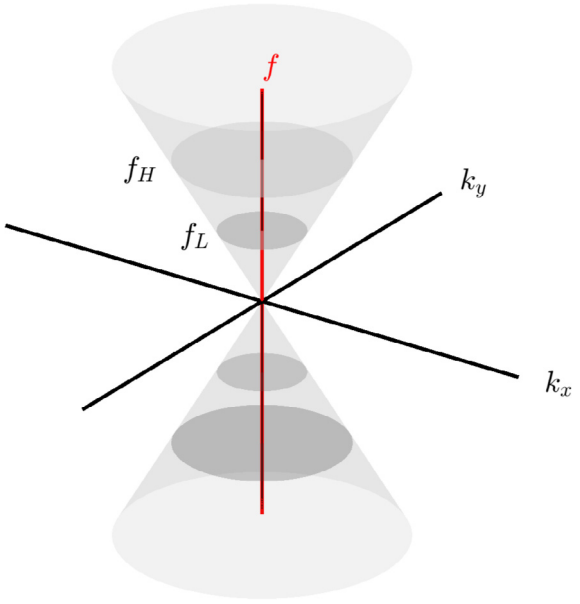


Fig. 7. Schematic representation of reflection data in the Fourier domain. All acquired data are restricted to a cone around the frequency axis. The lateral surface of the solid cone depends on the maximum aperture angle θ_{max} and determines at every frequency the maximum wavenumber that needs to be sampled in order to acquire un-aliased data.

interior using known techniques appropriate for complex models, e.g. time-domain finite-differences.

The practical consequence of all techniques discussed in this section is that the radar data acquired by a monostatic orbiter system can be imaged at once (consequence of the exploding reflector model) and starting from the known nucleus surface (consequence of wavefield redatuming). Given this significant compression of the problem to a global experiment strictly confined to the comet volume, we can employ wavefield imaging techniques that are relatively costly, but capable of handling arbitrary model complexity. Assuming that the grid size reduces by a ratio of $10\times$ (a conservative estimate), the wavefield extrapolation cost reduces by a factor of $1000\times$.

4. Data sampling

Orbital radar imaging effectiveness depends on the availability of well-sampled reflection data. Observations accumulate over time as the spacecraft revolves around a spinning nucleus, and therefore the array on which we sample data becomes denser over time. Here we seek to quantify the sampling distance necessary to acquire un-aliased data at every point along the orbital surface. Our approach is three-dimensional, and therefore we evaluate sampling requirements along the entire orbital surface, and not only along acquisition tracks.

Following from Fourier theory, we can decompose wavefields of arbitrary complexity into plane wave components. One can describe the total scattered wavefield in the comet interior, or propagating from the comet to the orbiter, as a collection of plane waves.

Monochromatic plane waves can be defined by

$$u(x,y,z,t) = u_0 e^{2\pi i\left(k_x x + k_y y + k_z z - ft\right)}, \tag{1}$$

where the function u represents one component of a band-limited harmonic signal with frequencies between f_L and f_H, and u_0 characterizes the wavefield amplitude. The 3D wavenumber vector $\mathbf{k} = \{k_x, k_y, k_z\}$ is related to the frequency f and the propagation speed c which depends on the dielectric material properties by

$$|\mathbf{k}| = \frac{f}{c}. \tag{2}$$

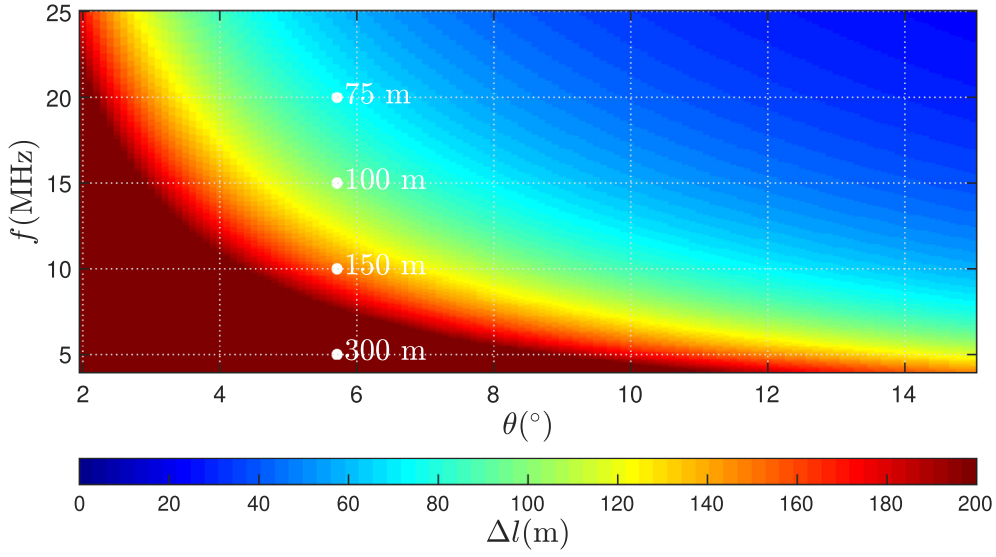


Fig. 8. Orbital sampling distance Δl needed to prevent aliasing of plane waves observed at the orbit altitude. The dots indicate sampling requirements at maximum propagation angles for $\{r, R\}$ pairs equal to $\{2.5, 25\}$ km or $\{0.25, 2.5\}$ km. For a given comet size, observations from a lower altitude require denser orbital sampling.

Following from Eq. (2), the magnitude of the wavenumber vector $\mathbf{k}$ is bound by $k_L = f_L/c$ and $k_H = f_H/c$.

Data sampling needs to satisfy the condition that all plane waves observed at the orbital array are un-aliased, both along and across the orbiter tracks. The key observation for sampling analysis is that plane waves propagate in free space at constant velocity $c = 0.3$ km/μs, and thus they maintain their direction unchanged for the entire time needed to travel from the comet to the orbiting spacecraft. Plane waves can therefore be characterized by their propagation direction measured by angle θ defined with respect to the radial direction (Fig. 5).

The maximum aperture angle θ_{max} at which plane waves could propagate from the nucleus to the spacecraft depends on the orbit altitude, and on the size and shape of the comet. Assuming that the comet cross-section has a mean size $2r$, and that the altitude of the orbiter from the comet center of mass is R, as depicted in Fig. 5, the maximum aperture angle is

$$\tan\theta_{max} = \frac{r}{R}. \tag{3}$$

There are no waves propagating at aperture angles greater than θ_{max}, since there are no radar scatterers outside the

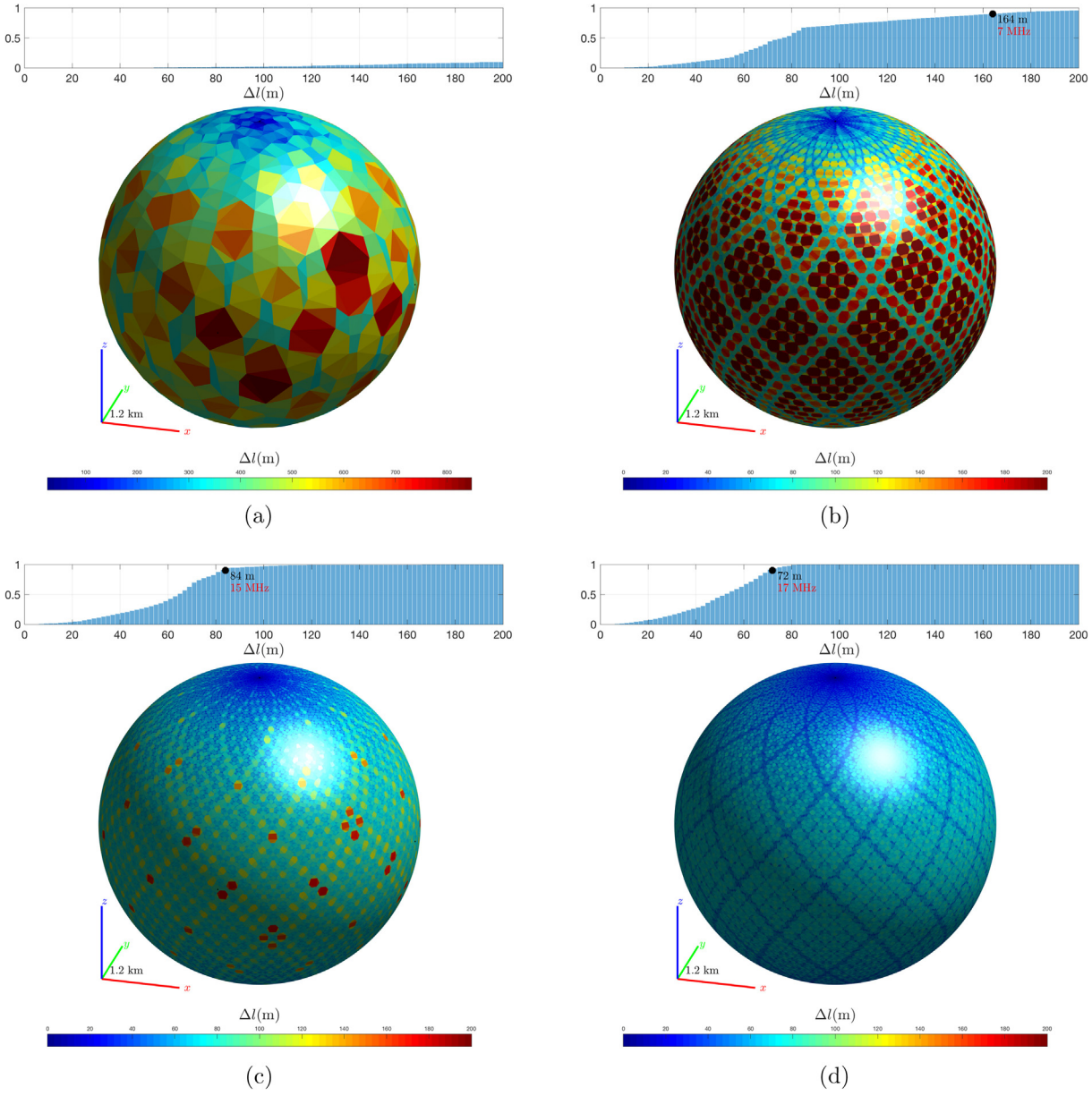


Fig. 9. (a) Triangulated surface generated using the spacecraft positions up to a set acquisition time. The color of each triangle depends on the diameter of its circumcircle, which is a proxy for sampling distance. Acquisition geometry performance as a function of time, for (b) 30 days, (c) 60 days and (d) 90 days. 90% of the acquisition surface is sampled at or better than the sampling distance marked on the histogram (black). The corresponding frequency that can be sampled un-aliased at a maximum aperture angle of $\theta_{max} = 7°$ increases with time (as indicated on the histogram in red). By definition, the entire comet nucleus is confined to the cone with the tip at the orbiter position and maximum aperture angle equal to θ_{max}, as depicted in Fig. 6. (For interpretation of the references to color in this figure legend, the reader is referred to the web version of this article.)

comet nucleus. The comet cross-section as seen from the orbiter changes with its position in orbit, therefore the maximum aperture angle changes along the orbit, Fig. 6. This angle represents the worst-case scenario, since $2r$ is the maximum lateral extent at which a comet nucleus is seen from a given position in orbit. Plane-wave components arriving at the orbital surface at angle θ_{max} require the densest sampling to avoid aliasing. We note that angle θ_{max} characterizes a circular cone, and therefore it is as large as needed to enclose the entire comet. For highly irregular comets, as for example depicted in Fig. 6(c), this angle may significantly overestimate the needed aperture.

A key sampling parameter is the distance between different measurement points in the cross-range directions measured *on the orbital surface, and not the comet surface*. Ground track spacing has no direct meaning for determining the ability of an orbital radar system to acquire unaliased data.

By definition, the observed data are simply the wavefield restricted to a given surface. In the far-field, i.e. more than 10 wavelengths away from the source, we can assume that the observation surface is approximately planar, and thus the observed data at distance R in the radial direction z can be derived from the wavefield defined in Eq. (1):

$$d(x,y,t) = u_0 e^{2\pi i\left(k_x x + k_y y + k_z R - ft\right)}. \tag{4}$$

Eq. (4) describes a plane wave in the x–y–t space, whose Fourier domain representation is a point that lies within a cone in the k_x–k_y–f space (Fig. 7) defined by

$$k(\theta) \equiv \sqrt{k_x^2 + k_y^2} = \frac{f}{c}\sin\theta, \tag{5}$$

where θ is the propagation angle at the observation surface relative to the radial direction. For the maximum propagation angle θ_{max} we obtain

$$k_{max} = \frac{f}{c}\sin\theta_{max}, \tag{6}$$

which is the maximum spatial wavenumber that needs to be acquired in order to record un-aliased monochromatic plane waves of frequency f propagating at angle θ_{max} relative to the radial direction. The corresponding spatial sampling distance that does not alias data up to the maximum wavenumber k_{max} given by Eq. (6) is

$$\Delta l \equiv \frac{1}{2k_{max}} = \frac{c}{2f\sin\theta_{max}}. \tag{7}$$

Using the wavelength $\lambda = c/f$, the sampling distance becomes

$$\Delta l = \frac{\lambda}{2\sin\theta_{max}}. \tag{8}$$

As a special case, Eq. (8) indicates that if we had to sample waves propagating directly along the orbital acquisition array, i.e. $\theta_{max} = 90^\circ$, then we would need to sample data at half wavelength distances, i.e. $\Delta l = \lambda/2$. This is not the case for the comet orbiter acquisition setup, for which the range of possible propagation angles is relatively small, e.g. $\sim 10^\circ$, depending on the comet size and orbiter altitude.

As seen in Fig. 8, depicting sampling distances as a function of propagation angles and frequencies, un-aliased

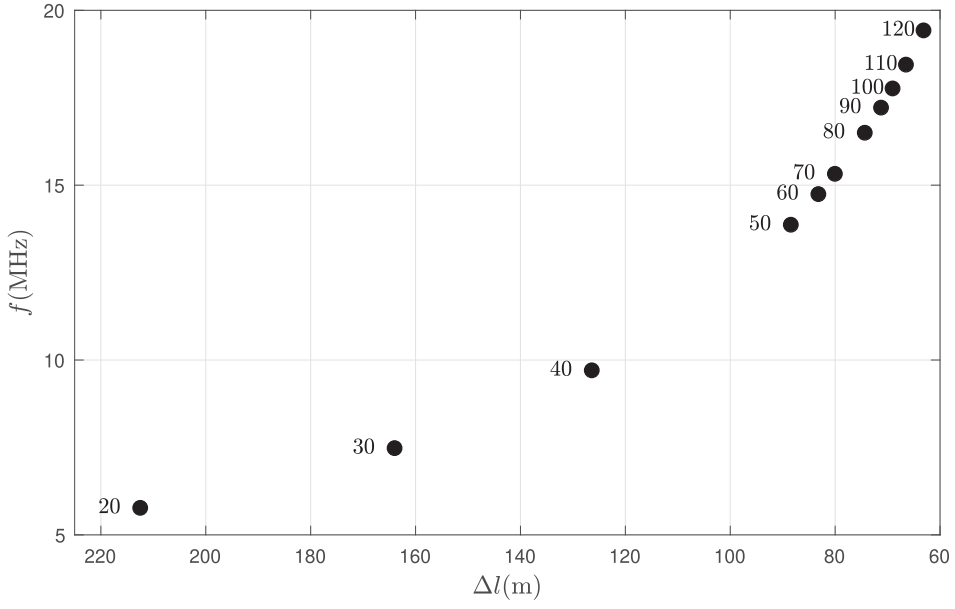


Fig. 10. 90th percentile unaliased frequency f as a function of the corresponding sampling distance Δl. Each represented $\{\Delta l, f\}$ pair corresponds to a different acquisition duration, as indicated next to each dot (in days). The sampling distance Δl decreases with acquisition duration, and thus the frequency f of the data that can be acquired (and imaged) without aliasing increases. Imaging can commence early in the mission with low-passed data, as indicated in the figure. Later in the mission, data can be imaged to increasingly higher frequencies. The variable imaging band does not influence acquisition, as data are acquired at all times in the widest band permitted by the radar instrumentation. Frequency filtering early in the mission is done just for imaging purposes.

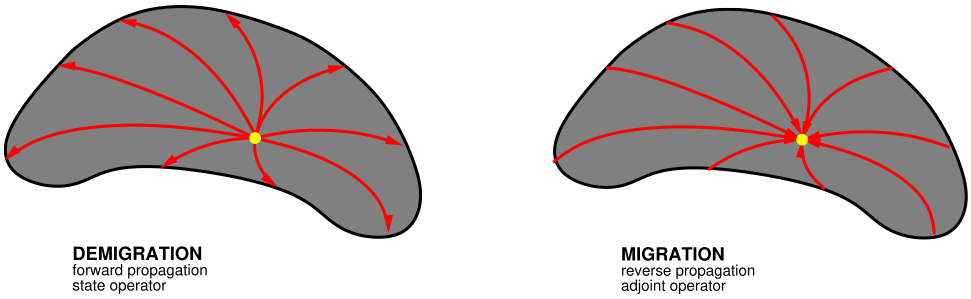


Fig. 11. (a) **Demigration**: waves from a scatterer in the comet interior are propagated forward in time and are collected on the comet surface. (b) **Migration**: waves observed on the comet surface are propagated backward in time and accumulate at the scatter. The rays are used just for conceptual illustration of wavefield extrapolation; in our method, all waves are extrapolated using time-domain finite differences.

sampling in the cross-range directions for frequencies up to 20 MHz is accomplished at altitude $R = 25$ km with the sampling distance $\Delta l = 75$ m for comet size $r = 2.5$ km, e.g. comet 67P/C-G. This sampling is significantly larger than the wavelength $\lambda/2 = 7.5$ m characteristic of a 20 MHz wave in free space. Lower wave frequencies can be sampled un-aliased with even coarser acquisition spacing.

5. Acquisition performance

The radar acquisition array consists of observation points on the orbital surface. These points are separated by variable distances Δl as a function of position, and also as a function of orbital acquisition (slow) time. As the observation time increases, the distances Δl reduce, thus increasing the performance of the orbital array. In the limit, the acquisition array is characterized by observation point separation distances Δl smaller than the sampling distance needed for un-aliased acquisition at every location along the orbital surface, as required by Eq. (7) and depicted in Fig. 6(d).

The question is what waves can we sample after a set acquisition time, i.e. what is the sampling performance as a function of time? One way to address this question is to evaluate characteristic distances between sampling points as a function of position and acquisition time. If we think of all acquisition points as nodes of a triangulated surface, we could use a characteristic size of each triangle to represent the sampling at its location. For example, we

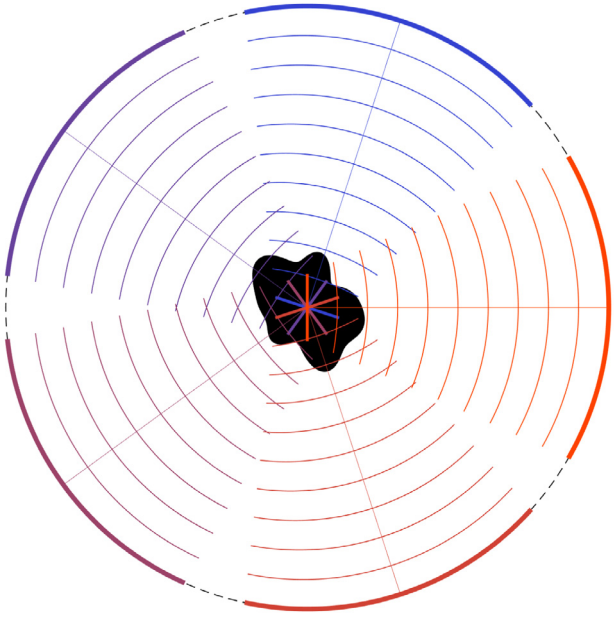


Fig. 12. Schematic representation of wavefield reconstruction at a scattering point in the interior of the comet. Plane waves radiating in all directions are sampled on the spherical orbital surface. Assuming that we know the propagation speed throughout the comet interior, we can reconstruct all plane waves at the scattering point using time-reversal. Many plane waves ($\sim 10^6$) are available for 3D reconstruction after appropriately long acquisition time.

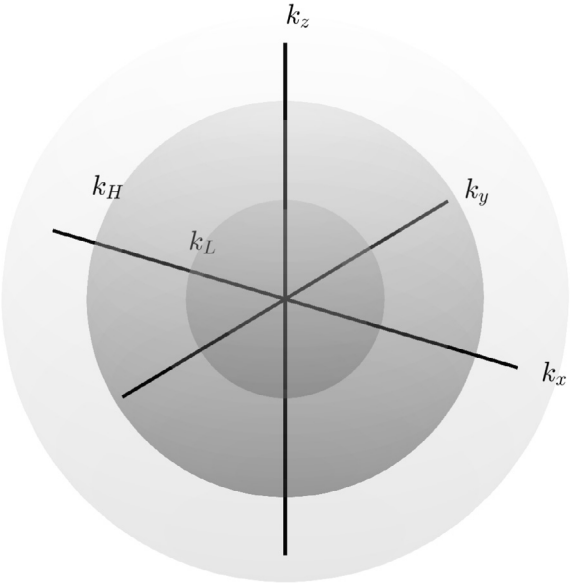


Fig. 13. Schematic representation of the image wavenumber space resulting from back-propagation of all recorded waves to their scattering positions. Since data are acquired all around the comet, i.e. 4π steradians acquisition, the wavenumbers for all propagation directions are represented by the entire space between the spheres corresponding to the data low and high frequencies.

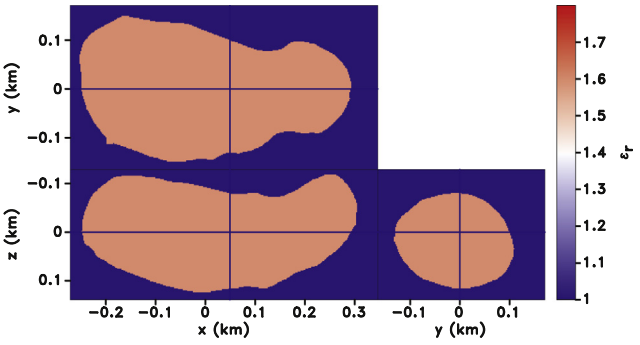


Fig. 14. Model used to illustrate migration and demigration.

could use the diameter of each triangle's circumcircle as a measure of overall sampling distance at the location of that specific triangle, Fig. 9(a). This option represents a worst-case scenario, since by definition each triangle's sides are smaller than the diameter of the circumcircle. This measure, therefore, systematically underestimates the actual sampling performance, but it can serve as a conservative benchmark.

The dimensions of the triangles characterizing the acquisition surface decrease progressively over time, and therefore the effective sampling distances reduce proportionally. For example, Fig. 9(b)–(d) demonstrate the orbital performance for the setup in Fig. 2 as a function

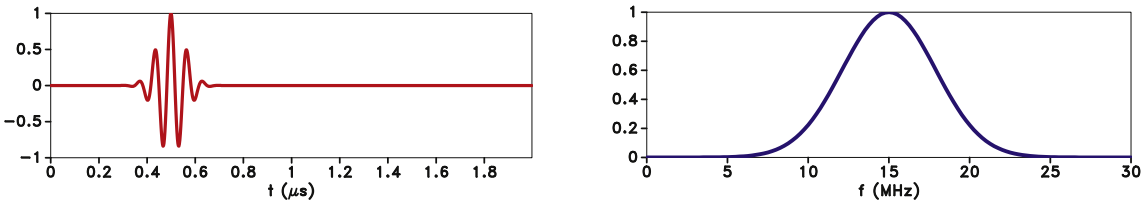


Fig. 15. (a) Compressed wavelet, and (b) its Gaussian amplitude spectrum.

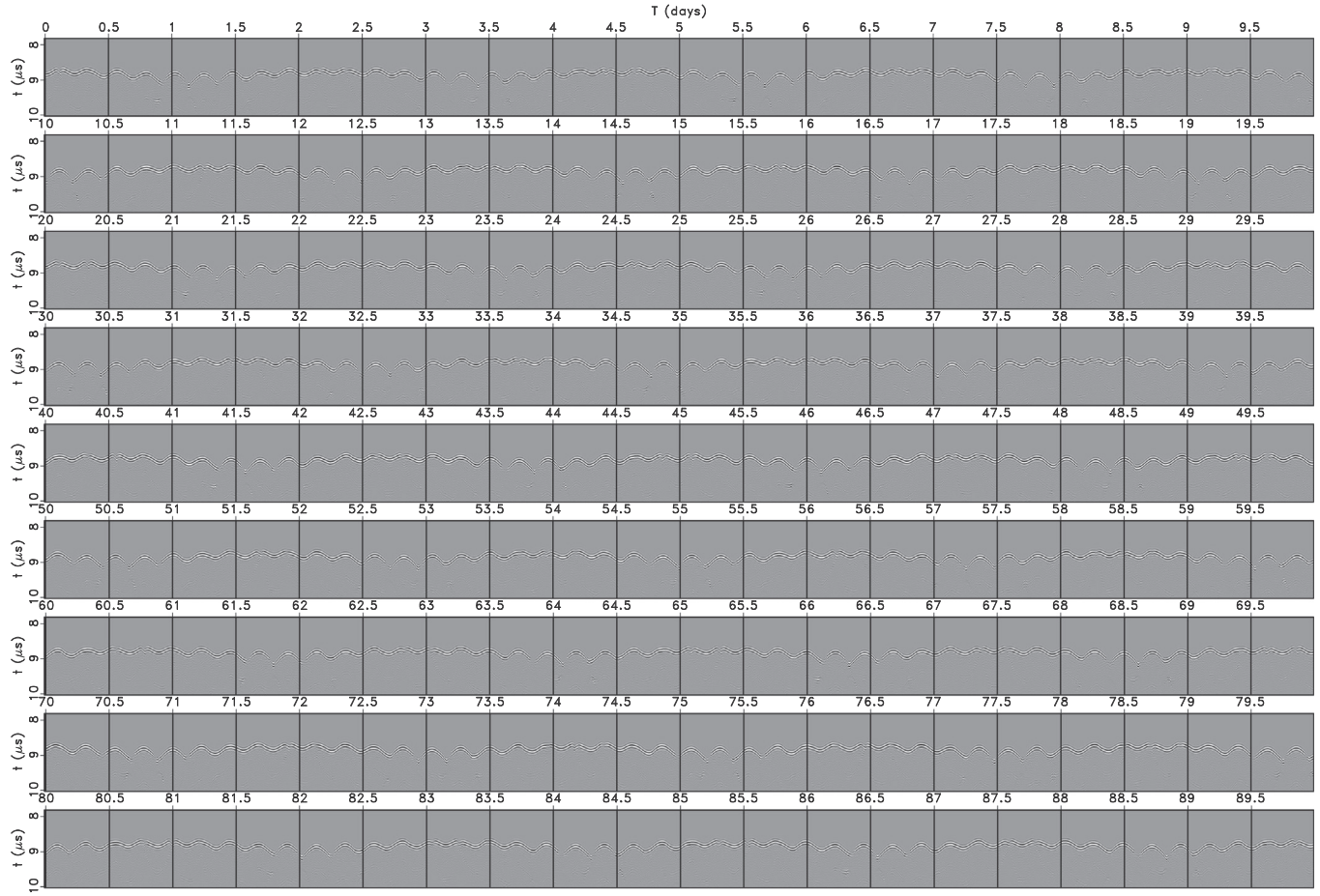


Fig. 16. One-way radar data corresponding to a single scatterer in the comet interior and 90 days of orbital acquisition at a radius of 2.5 km. The variable T (days) represents orbiter (slow) time, and the variable t (μs) represents reflection (fast) time.

of acquisition (slow) time, for 30, 60 and 90 days, respectively.

Furthermore, we can evaluate the acquisition performance globally with the 90th percentile sampling distance, Δl_{90}. Using this specific distance, we can estimate the corresponding frequency, f_{90} at the maximum aperture angle θ_{max}:

$$f_{90} = \frac{c}{2\Delta l_{90} \sin\theta_{max}}. \tag{9}$$

Eq. (9) indicates that 90% of the radar measurements are un-aliased up to the frequency f_{90}. As Δl_{90} reduces over time, the top un-aliased frequency f_{90} increases, and so does the image bandwidth. Fig. 10 depicts the maximum data frequency f that can be sampled un-aliased as a function of acquisition time. Only lower frequencies can be imaged early in the mission, given the relatively coarse acquisition array. As the acquisition array density increases, data can be imaged up to increasingly higher frequencies. Acquisition is not influenced by the variable frequency band; data are always acquired in the full band of the radar system.

6. Reverse time migration

The goal of **wavefield migration** is to generate an image of the reflectors responsible for the observed data. We are considering data transformed to one-way traveltime under the logic of the exploding reflector model, explained earlier. An effective description of migration exploits properties of linear operators relating observed data and migrated images.

The definition of migration derives from the definition of its adjoint process, i.e. demigration, which is characterized by a linear operator $\mathcal{M}$ relating the observed data $\mathbf{d}(\mathbf{r}, t)$ and the migrated image $\mathbf{i}(\mathbf{x})$:

$$\mathbf{d} = \mathcal{M}\mathbf{i}. \tag{10}$$

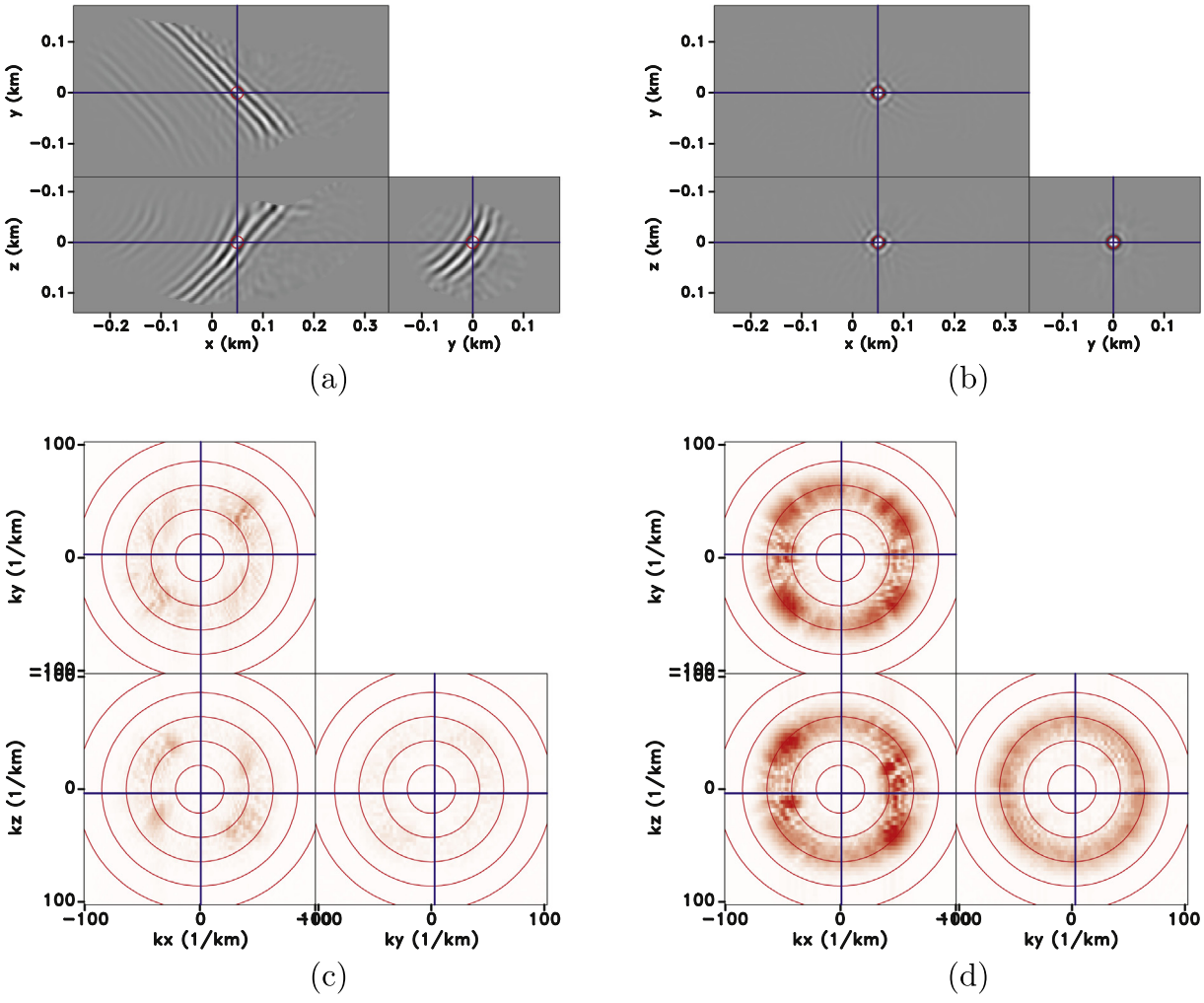


Fig. 17. Reverse time migration for (a)–(c) a single illumination direction and (b)–(d) all illumination directions. Panels (a)–(b) depict the RTM image in the space domain, and panels (c)–(d) depict the RTM image in the wavenumber domain. The red circular overlays in (a)–(b) indicate the expected image range resolution derived from the data bandwidth. The red concentric circles overlay in (c)–(d) indicate wavenumbers corresponding to frequencies from 5 to 25 MHz, in increments of 5 MHz. (For interpretation of the references to color in this figure legend, the reader is referred to the web version of this article.)

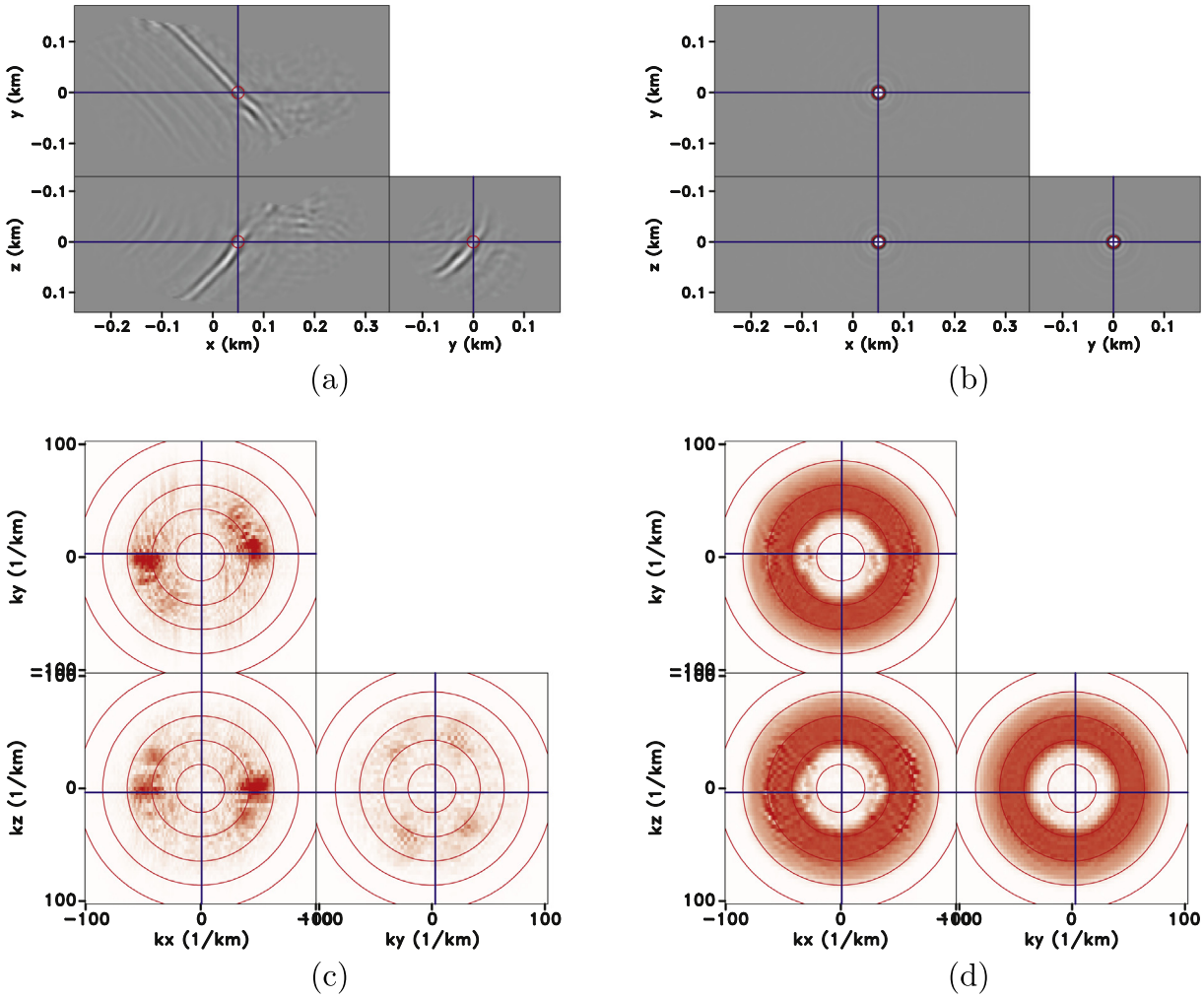


Fig. 18. Least-squares migration for (a)–(c) a single illumination direction and (b)–(d) all illumination directions. Panels (a)–(b) depict the LSM image in the space domain, and panels (c)–(d) depict the LSM image in the wavenumber domain. The red circular overlays indicate the expected image range resolution derived from the data bandwidth. (For interpretation of the references to color in this figure legend, the reader is referred to the web version of this article.)

Here, $\mathbf{x}$ represents coordinates in the comet interior, t represents one-way time, and $\mathbf{r}$ are coordinates where data are available for imaging, i.e. the comet surface to which all data from the orbital acquisition surface have been datumed.

The demigration (forward) operator $\mathcal{M}$, Fig. 11(a), consists of three main components:

F1: *Source synthesis*, characterized by a linear operator $\mathcal{S}$ which incorporates the radar wavelet. Its purpose is to generate the exploding reflector source $\mathbf{s}(\mathbf{x},t)$ by time convolution of the radar wavelet $w(t)$ with the reflectivity described as a function of space $\mathbf{i}(\mathbf{x})$ at zero time:

$$\mathbf{s} = \mathcal{S}\,\mathbf{i}. \tag{11}$$

F2: *Wavefield forward propagation*, also characterized by a linear operator $\mathcal{W}$. The purpose of this operator is to extrapolate the source function $\mathbf{s}(\mathbf{x},t)$ forward in time, thus generating the wavefield $\mathbf{u}(\mathbf{x},t)$ at every time t and location $\mathbf{x}$ in the interior of the comet:

$$\mathbf{u} = \mathcal{W}\,\mathbf{s}. \tag{12}$$

F3: *Data extraction*, also characterized by a linear operator $\mathcal{K}$, whose purpose is to extract the data $\mathbf{d}(\mathbf{r},t)$ from the wavefield $\mathbf{u}(\mathbf{x},t)$ at the observation locations:

$$\mathbf{d} = \mathcal{K}\,\mathbf{u}. \tag{13}$$

With these definitions, we can describe demigration as

$$\mathbf{d}(\mathbf{r},t) = \mathcal{K}\mathcal{W}\mathcal{S}\,\mathbf{i}(\mathbf{x}), \tag{14}$$

and therefore we can write the **demigration operator** $\mathcal{M}$ as a chain of three linear operators:

$$\mathcal{M} = \mathcal{K}\mathcal{W}\mathcal{S}. \tag{15}$$

Conversely, we can write the **migration operator** $\mathcal{M}^\top$ as a chain of the adjoints of the same three linear operators:

$$\mathcal{M}^\top = \mathcal{S}^\top \mathcal{W}^\top \mathcal{K}^\top, \tag{16}$$

assembled in adjoint order. Therefore, we can describe migration as

$$\mathbf{i}(\mathbf{x}) = \mathcal{S}^\top \mathcal{W}^\top \mathcal{K}^\top \, \mathbf{d}(\mathbf{r}, t). \tag{17}$$

The migration (adjoint) operator $\mathcal{M}^\top$, Fig. 11(b), consists of three main components:

A3: *Data injection*, described by the adjoint of the linear operator $\mathcal{K}$, whose purpose is to inject the observed data $\mathbf{d}(\mathbf{r}, t)$ into the wavefield $\mathbf{u}(\mathbf{x}, t)$ at the observation locations $\mathbf{r}$

$$\mathbf{u} = \mathcal{K}^\top \, \mathbf{d}. \tag{18}$$

A2: *Wavefield reverse propagation*, characterized by the adjoint of the linear operator $\mathcal{W}$. The purpose of this operator is to extrapolate backward in time the wavefield $\mathbf{u}(\mathbf{x}, t)$ in order to generate the scattered wavefield $\mathbf{s}(\mathbf{x}, t)$ at all times t and every location $\mathbf{x}$ in the comet interior:

$$\mathbf{s} = \mathcal{W}^\top \, \mathbf{u}. \tag{19}$$

A1: *Imaging condition*, characterized by the adjoint of the synthesis linear operator $\mathcal{S}$. Its purpose is to generate the image $\mathbf{i}(\mathbf{x})$ as the zero-lag correlation between the source wavelet $w(t)$ and the scattered wavefield $\mathbf{s}(\mathbf{x}, t)$:

$$\mathbf{i} = \mathcal{S}^\top \, \mathbf{s}. \tag{20}$$

Wavefield imaging with the adjoint operator $\mathcal{M}^\top$

$$\mathbf{i}_{RTM} = \mathcal{M}^\top \mathbf{d}. \tag{21}$$

is known as **reverse time migration** (RTM) (Kosloff and Baysal, 1983; McMechan, 1983; Lailly, 1983), since it is based on wavefield propagation backward in time to reconstruct the reflectivity at every location in the comet interior from the observed data.

The central component of reverse time migration is the extrapolation operator $\mathcal{W}$ which incorporates the physical relations governing electromagnetic wave propagation, as well as the dielectric medium parameters: permeability $\mu(\mathbf{x})$, permittivity $\epsilon(\mathbf{x})$, and conductivity $\sigma(\mathbf{x})$. The extrapolation operator is linear relative to the model parameters, which therefore function simply as parameters in the definition of the operator itself:

$$\mu\epsilon \frac{\partial^2 u}{\partial t^2} + \mu\sigma \frac{\partial u}{\partial t} - \nabla^2 u = s. \tag{22}$$

The field and source quantities, $u(\mathbf{x}, t)$ and $s(\mathbf{x}, t)$, change roles for the adjoint operator $\mathcal{W}^\top$.

As discussed earlier, the model parameters are presumed known during migration, as they are derived using the complementary process of wavefield tomography (Sava and Asphaug, 2018). This is the main reason why we can describe migration using linear operators. We emphasize that more sophisticated physics accounting for vector wavefields and polarization changes during wave propagation can be incorporated in operator $\mathcal{W}$, with no change to the overall framework discussed here. We leave a detailed discussion of other known extrapolation operators outside the scope of this paper.

Finally, we re-emphasize that migration acts on data available on the comet surface after datuming the data

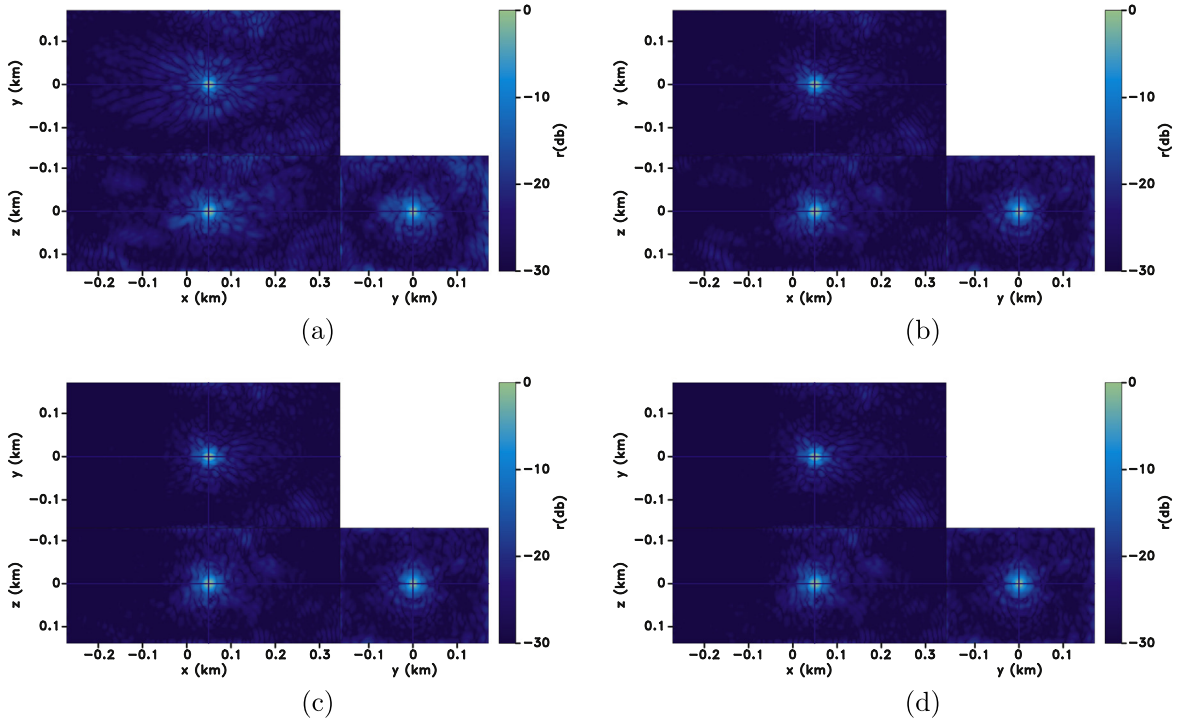


Fig. 19. Migrated images for 10, 30, 60 and 90 days of acquisition (slow) time. All images are represented in dB scale to emphasize low amplitude artifacts.

collected on the orbital surface, thus significantly reducing its computational cost.

7. Migration resolution

We can analyze migration resolution by measuring its ability to image a point scatterer at an arbitrary location inside the comet using a band-limited wave. By definition, scatterers radiate waves in all directions, which are recorded by the orbital radar array. Assuming sufficient penetration depth in the comet interior, all waves scattered at a point can propagate to the comet surface, and thus to the orbital array. We can therefore safely assume that in this problem we capture scattered waves on a spherical orbital surface, which is equivalent to SAR imaging the interior of the comet with a 4π steradians synthetic aperture. This observation has profound consequences for the image spatial resolution.

Plane waves sampled without aliasing can be reconstructed at their original position and trigger time using time-reversal (Fink et al., 2002), Fig. 12. The migration imaging condition, zero time-lag of the wavefield cross-correlation with the radar wavelet, highlights the locations of plane waves back-propagated to their scattering time. The image is, therefore, a subset of the wavefield at zero time:

$$i(x,y,z) = u_0 e^{2\pi i\left(k_x x + k_y y + k_z z\right)} \tag{23}$$

Eq. (23) describes a plane in the x–y–z space, whose wavenumber domain representation is a line oriented in the direction of the wavenumber vector $\mathbf{k} = \{k_x, k_y, k_z\}$. Given illumination from all directions, a scatterer is bounded in the wavenumber domain by two concentric spheres with radii defined by the wavenumbers k_L and k_H related to the low and high data frequencies, Fig. 13.

The wavenumbers k_L and k_H constrain the expected imaging resolution. Defining the frequency and wavenumber bandwidths by $B_f = f_H - f_L$ and $B_k = k_H - k_L$, respectively, then the image resolution B_i is defined by

$$B_i = \frac{1}{B_k} = \frac{v}{B_f}, \tag{24}$$

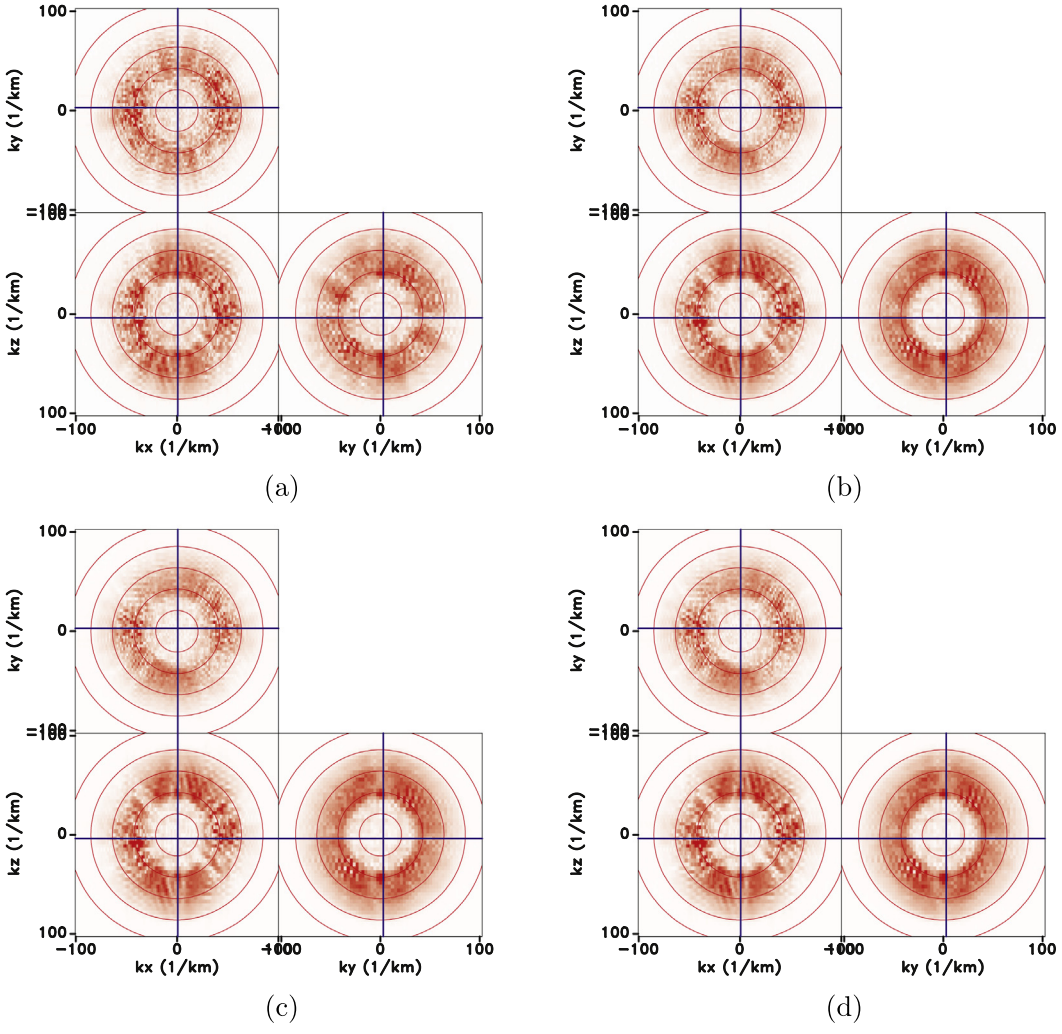


Fig. 20. Wavenumber representations of the images shown in Fig. 19 for 10, 30, 60 and 90 days of acquisition (slow) time, respectively.

where $v < c$ represents the imaging velocity in the comet interior. Since the velocity changes as a function of position, the imaging resolution changes accordingly. This measure of resolution is a consequence of the Fourier transform spreading property: the spread of a signal in one domain (e.g. space) is reciprocal to its spread in the transform domain (e.g. wavenumber). Eq. (24) is consistent with radar range resolution formulas (Curlander and McDonough, 1991; Richards, 2014), but accounts for the one-way propagation characterizing the exploding reflector model.

The theoretical image resolution is identical in all directions, regardless of the position of the scatter in the interior of the comet. For time-reversal imaging using the full spherical aperture characteristic of the comet imaging problem, the concepts of horizontal and vertical resolution do not apply. The image resolution is the same in all directions, and it is equivalent with the radar range resolution mapped to space at every point through the local propagation velocity.

For illustration of migration and demigration, consider the comet model in Fig. 14 built using the shape of asteroid 25143 Itokawa. The figure depicts a model with constant interior velocity 0.237 km/μs, corresponding to a relative dielectric permittivity $\epsilon_r = 1.59$. We use the compressed radar wavelet shown in Fig. 15(a), which has the Gaussian amplitude spectrum depicted in Fig. 15(b). We choose this wavelet with peak frequency of 15 MHz and 10 MHz bandwidth in order to obtain a relatively narrow wavelet with reduced side-lobes. In order to demonstrate imaging resolution, we consider a reflectivity model consisting of a single scatterer at coordinates $\{x, y, z\} = \{0.05, 0, 0\}$ km. The one-way data corresponding to this scatterer and 90 days of orbital radar acquisition are shown in Fig. 16.

Fig. 17(a) depicts the 3D migrated image for a single position of the orbiting spacecraft. As discussed earlier, the image corresponding to this point is approximately a plane whose orientation depends on the spacecraft position, but also on the comet shape and material properties. The diameter of the circular overlay indicates the expected resolution given the data bandwidth and interior velocity. Fig. 17(c) depicts the image in Fig. 17(a) transformed to the wavenumber domain. The circular overlay represents wavenumbers for frequencies $f = 5 - 25$ MHz, in increments of 5 MHz. The image resolution in the direction connecting the scatterer and the spacecraft is large, while the resolution in the orthogonal direction is low. In contrast to Fig. 17(a), Fig. 17(b) represents the image obtained for waves propagating in all directions around the scatterer. In this case, the image resolution is the same in all directions, and equivalent to the radar range resolution. Fig. 17(d) represents the image in Fig. 17(b) transformed to the wavenumber domain. The images in Fig. 17(a) and (b) represent the migration point spread functions for a single and all possible propagation directions around the scatterer, respectively, resulting from the successive application of the demigration and migration operators.

8. Least-squares migration

An effective way to control and increase migration resolution exploits the concept of **point spread functions**. Consider a reflectivity model consisting of a single impulse at an arbitrary location in the comet interior. The scattered data $\mathbf{d}(\mathbf{r}, t)$ are formed by the application of the demigration operator $\mathcal{M}$ to the reflectivity $\boldsymbol{\delta}(\mathbf{x})$:

$$\mathbf{d} = \mathcal{M}\,\boldsymbol{\delta}. \tag{25}$$

Similarly, the migrated image $\mathbf{i}(\mathbf{x})$ is formed by the application of the migration operator $\mathcal{M}^\top$ to the data $\mathbf{d}(\mathbf{r}, t)$:

$$\mathbf{i} = \mathcal{M}^\top \mathbf{d} \tag{26}$$

$$= \mathcal{M}^\top \mathcal{M}\,\boldsymbol{\delta}. \tag{27}$$

Through the cascade application of the demigration and migration operators we recover an image $\mathbf{i}$ which differs from the original reflectivity model $\boldsymbol{\delta}$. This recovered image defines the migration point spread function, as it is formed by the convolution of blurring the original spike with the point spread function $\mathcal{M}^\top\mathcal{M}$. The amount of blur describes the imaging resolution, and it is related to the radar wavelet embedded in the demigration and migration operators.

As discussed earlier, reverse time migration is based on the application of the migration operator to the data datumed to the comet surface. The migration operator is, by definition, the adjoint to the demigration operator

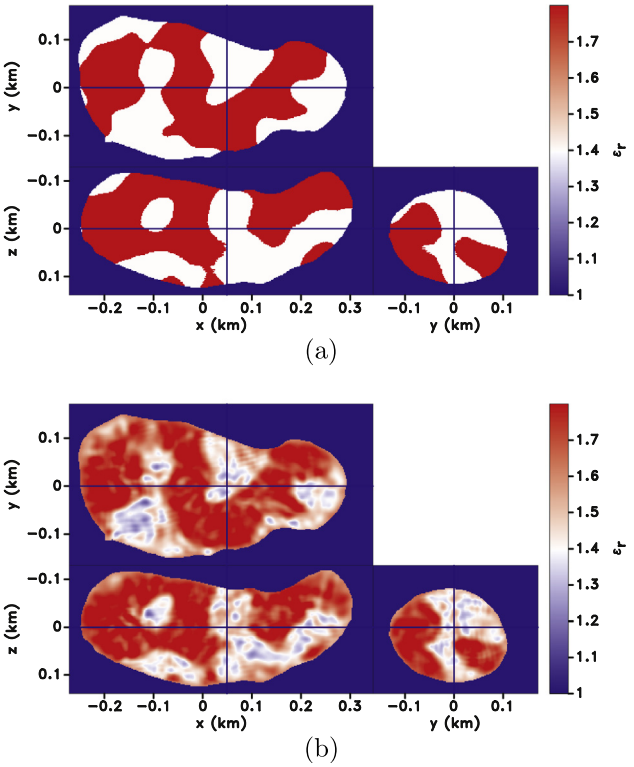


Fig. 21. (a) True comet model and (b) model recovered by wavefield tomography.

which relates the reflectivity image with the data. Migration is not the inverse of demigration, and therefore it cannot remove the bandwidth blur caused by the source wavelet.

However, an extension to reverse time migration, known as **least-squares migration** (LSM) (Chavent and Plessix, 1999; Nemeth et al., 1999; Aoki and Schuster, 2009; Dai et al., 2012), can reduce the blur caused by the migration point spread function on the image, leading to higher image resolution. Least-squares migration, forms an image by solving an inverse problem based on minimizing the objective function

$$J(\mathbf{i}) = \frac{1}{2}\|\mathbf{d} - \mathcal{M}\,\mathbf{i}\|^2 \tag{28}$$

with respect to the image $\mathbf{i}$.

By minimizing this objective function, we obtain an image that best explains in a least-squares sense the observed data through the demigration operator $\mathcal{M}$:

$$\mathbf{i}_{LSM} = \left(\mathcal{M}^\top\mathcal{M}\right)^{-1}\mathcal{M}^\top\,\mathbf{d}. \tag{29}$$

Least-squares migration has two components:

- $\mathcal{M}^\top\mathbf{d}$ is the reverse time migration image, Eq. (21).
- $\mathcal{M}^\top\mathcal{M}$ is the point spread function, Eq. (26).

The $\left(\mathcal{M}^\top\mathcal{M}\right)^{-1}$ operator has the purpose of whitening the spectrum of the migrated image, thus sharpening the RTM image, Eq. (21), by increasing its spatial resolution to the maximum extent allowed by the data bandwidth. In practice, this operator is never explicitly formed, rather inverting the point spread function is accomplished through an iterative process, e.g. by the conjugate gradient method, that achieves convergence after a number of iterations at most equal to the number of image points. This process is not run to convergence, yet a significant component of the migration point spread function is removed during the early iterations, leading to higher resolution than what would be expected from conventional wavelet analysis.

Fig. 18(a) and (b) depict the least-squares migrated images for illumination of the scatterer in a single direction (corresponding to Fig. 17(a)), or all possible directions (corresponding to Fig. 17(b)). The wavelet deconvolution executed by least-squares migration flattens the image spectrum, as seen in Fig. 18(c) and (d), and thus compresses the image wavelet compared with reverse time migration, Fig. 17(c) and (d).

Fig. 19 shows the evolution of the image for a single scatterer as a function of acquisition (slow) time for $10, 30, 60$ and 90 days, respectively. All images are presented in dB scale in order to emphasize the low amplitude

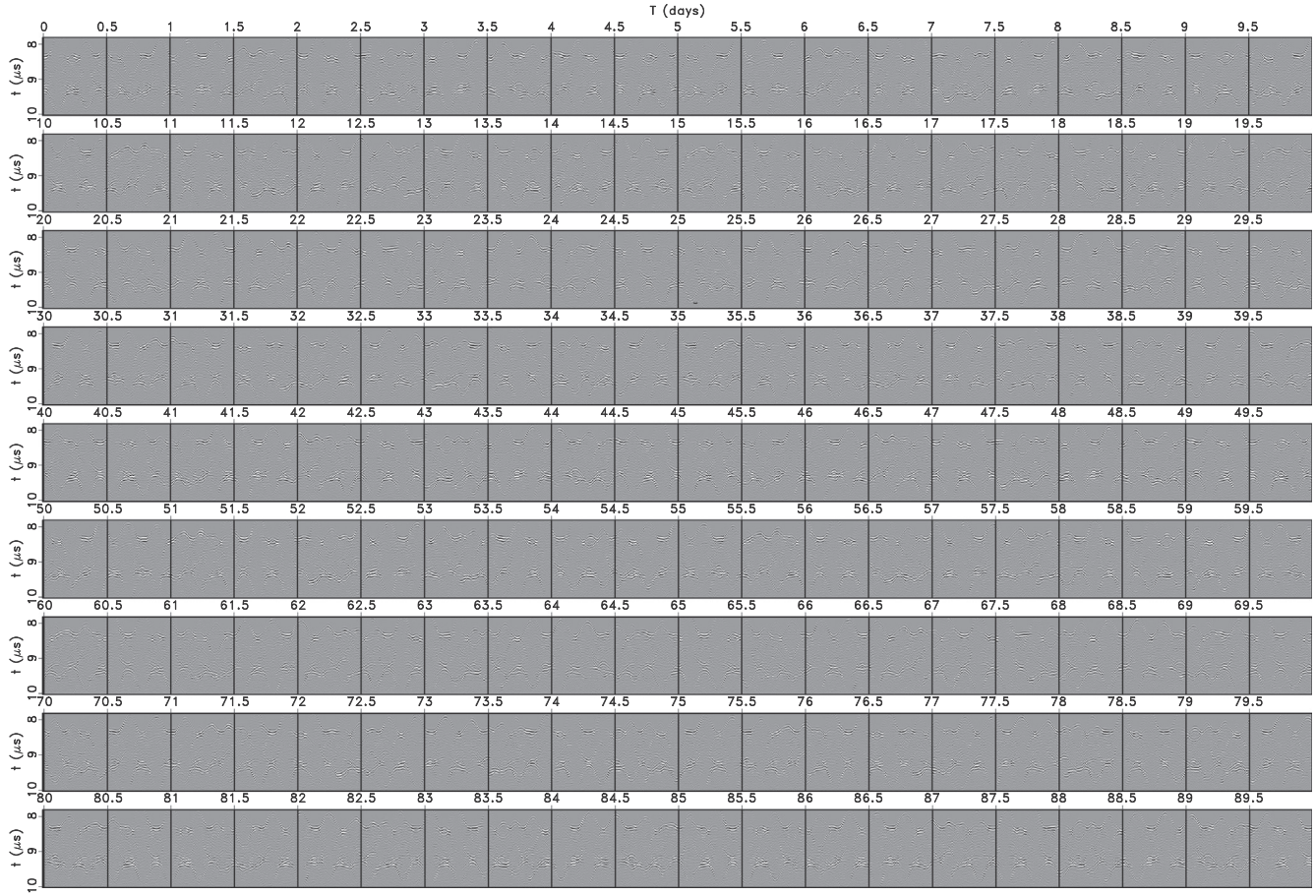


Fig. 22. One-way radar data corresponding to the model depicted in Fig. 21(a) and 90 days of orbital acquisition at a radius of 2.5 km. Variable T (days) represents acquisition (slow) time, and variable t (μs) represents reflection (fast) time.

artifacts. As discussed earlier, the density of acquisition points increases as a function of slow time, and consequently the imaging artifacts reduce progressively. Fig. 20 further emphasizes the progressive artifact reduction with wavenumber representations of the images in Fig. 19. The amplitude spectra of the migrated images converge progressively to the ideal case (full, dense sampling of the acquisition surface) depicted in Fig. 17(d).

9. Example

We illustrate the wavefield migration approach with the model depicted in Fig. 21(a). This model consists of two materials with relative dielectric permittivity ϵ_r of 1.8 and 1.4, representing different types of ice (Stillman et al., 2010). These permittivities convert to electromagnetic wave speeds of 0.22 and 0.25 km/μs, respectively.

Simulated radar reflection data for 90 days of orbital acquisition are depicted in Fig. 22. The two main visible arrivals correspond to reflections from the near and far comet surfaces, respectively. Other interior reflections are visible, but cannot be easily positioned in the comet.

Fig. 21(b) depicts the relative dielectric permittivity recovered using multi-scale 3D wavefield tomography as discussed in Sava and Asphaug (2018). Using these material properties, reverse time migration, Fig. 23(a), positions the major reflectors in the comet interior, but without the correct amplitude response. In contrast, least-squares migration, Fig. 23(b), recovers correct reflection amplitudes, and high imaging resolution. As discussed earlier, the image resolution is the same in all directions, given the complete radar acquisition surrounding the comet nucleus.

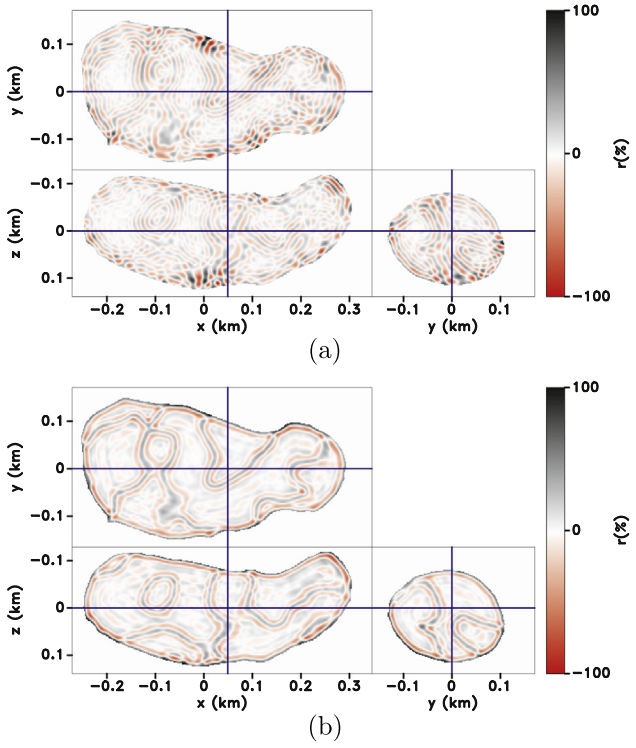


Fig. 23. (a) RTM image and (b) LSM image for the model depicted in Fig. 21. The scale bar represents normalized reflectivity.

10. Conclusions

A three-dimensional geologic structural map of a primitive body is of inestimable significance to planetary science. These objects are relics from the beginning of the Solar System, so knowing their interior structure would relate to us the story of how they were put together and how they have evolved collisionally and thermodynamically.

Reverse time migration applied to data acquired by a monostatic radar orbiter can generate high resolution images of comet nuclei interior. In our formulation, migration is essentially equivalent to synthetic aperture radar imaging, with three main enhancements:

1. The imaging synthetic aperture is as wide as the entire orbital acquisition surface, i.e. 4π steradians. Such wide aperture leads to 3D image resolution commensurate with the radar range resolution in all directions. Least-squares migration further increases the resolution by deconvolving the radar wavelet from the image.
2. Unlike conventional SAR processing, migration propagates wavefields through models of arbitrary complexity, thus accurately accounting for wavefield deflection by heterogeneous dielectric properties. The wave propagators formulated, e.g., by time-domain finite-differences are robust and applicable to comets with arbitrary shapes and distribution of physical properties in their interior.
3. The sampling requirements for unaliased data are significantly less stringent than half wavelength, given the radar acquisition with a monostatic orbiter at a relatively large distance from the comet nucleus. The radar data acquired in orbit can be efficiently relocated to the known comet surface through wavefield datuming, thus significantly reducing the imaging computational cost.

Acknowledgment

This work was conducted with support from the Center for Wave Phenomena at Colorado School of Mines. The reproducible numeric examples in this paper use the Madagascar open-source software package (Fomel et al., 2013), freely available from www.ahay.org.

References

Aki, K., Richards, P., 2002. Quantitative Seismology, second ed. University Science Books.

Aoki, N., Schuster, G., 2009. Fast least-squares migration with a deblurring filter. Geophysics, WCA83–WCA93.

Asphaug, E., Barucci, A., Belton, M., Bhaskaran, S., Brownlee, D., Carter, L., Castillo, J., Chelsey, S., Chodas, P., Farnham, T., Gaskell, R., Gim, Y., Heggy, E., Klaasen, K., Kofman, W., Krelavsky, M., Lisse, C., McFadden, L., Pettinelli, E., Plaut, J., Scheeres, D., Turtle, E., Weissman, P., Wu, R., 2010. Deep interior radar imaging of comets. In: Lunar and Planetary Science Conference, pp. 2670.

Batygin, K., Laughlin, G., Morbidelli, A., 2016. The violent biography of our solar system. Sci. Am., 33–41

Belton, M.J., Thomas, P., Veverka, J., Schultz, P., A'Hearn, M.F., Feaga, L., Farnham, T., Groussin, O., Li, J.-Y., Lisse, C., McFadden, L., Sunshine, J., Meech, K.J., Delamere, W.A., Kissel, J., 2007. The internal structure of Jupiter family cometary nuclei from Deep Impact observations: the "talps" or "layered pile" model. Icarus 187 (1), 332–344.

Berkhout, A.J., 1982. Imaging of Acoustic Energy by Wave Field Extrapolation. Elsevier.

Cafforio, C., Prati, C., Rocca, F., 1991. SAR data focusing using seismic migration techniques. IEEE Trans. Aerospace Electron. Syst. 27 (2), 194–207.

Capria, M.T., Capaccioni, F., Filacchione, G., Tosi, F., De Sanctis, M.C., Mottola, S., Ciarniello, M., Formisano, M., Longobardo, A., Migliorini, A., Palomba, E., Raponi, A., Kührt, E., Bockelée-Morvan, D., Erard, S., Leyrat, C., Zinzi, A., 2017. How pristine is the interior of the comet 67P/Churyumov-Gerasimenko?. Mon. Not. R. Astron. Soc. 469 (Suppl 2) S685–S694.

Chavent, G., Plessix, R., 1999. An optimal true-amplitude least-squares prestack depth-migration operator. Geophysics, 508–515.

Ciarletti, V., Herique, A., Lasue, J., Levasseur-Regourd, A.-C., Plettemeier, D., Florentin, L., Christophe, G., Pierre, P., Kofman, W., 2017. CONSERT constrains the internal structure of 67P at a few-metre size scale. Mon. Not. R. Astron. Soc., stx3132

Clærbout, J.F., 1985. Imaging the Earth's Interior. Blackwell Scientific Publications.

Curlander, J., McDonough, R., 1991. Synthetic Aperture Radar: Systems and Signal Processing. Wiley.

Dahlen, F.A., Tromp, J., 1998. Theoretical Global Seismology. Princeton University Press.

Dai, W., Fowler, P., Schuster, G., 2012. Multi-source least-squares reverse time migration. Geophys. Prospect. 60 (4), 681–695.

El-Maarry, M.R., Thomas, N., Giacomini, L., Massironi, M., Pajola, M., Marschall, R., Gracia-Berná, A., Sierks, H., Barbieri, C., Lamy, P.L., Rodrigo, R., Rickman, H., Koschny, D., Keller, H.U., Agarwal, J., A'Hearn, M.F., Auger, A.-T., Barucci, M.A., Bertaux, J.-L., Bertini, I., Besse, S., Bodewits, D., Cremonese, G., Da Deppo, V., Davidsson, B., De Cecco, M., Debei, S., Güttler, C., Fornasier, S., Fulle, M., Groussin, O., Gutierrez, P.J., Hviid, S.F., Ip, W.-H., Jorda, L., Knollenberg, J., Kovacs, G., Kramm, J.-R., Kührt, E., Küppers, M., La Forgia, F., Lara, L.M., Lazzarin, M., Lopez Moreno, J.J., Marchi, S., Marzari, F., Michalik, H., Naletto, G., Oklay, N., Pommerol, A., Preusker, F., Scholten, F., Tubiana, C., Vincent, J.-B., 2015. Regional surface morphology of comet 67P/Churyumov-Gerasimenko from Rosetta/OSIRIS images. Astron. Astrophys. 586, A26.

Fink, M., Kuperman, W., Montagner, J.-P., 2002. Imaging of Complex Media with Acoustic and Seismic Waves. Springer.

Fomel, S., Sava, P.C., Vlad, I., Liu, Y., Bashkardin, V., 2013. Madagascar: open-source software project for multidimensional data analysis and reproducible computational experiments. J. Open Res. Softw. 1 (1), e8.

Foss, F.J., Putzig, N.E., Campbell, B.A., Phillips, R.J., 2017. 3D imaging of Mars' polar ice caps using orbital radar data. Lead. Edge 36 (1), 43–57.

Heggy, E., Palmer, E.M., Kofman, W., Clifford, S.M., Righter, K., Hérique, A., 2012. Radar properties of comets: parametric dielectric modeling of comet 67P/Churyumov-Gerasimenko. Icarus 221 (2), 925–939.

Jol, H., 2008. Ground Penetrating Radar Theory and Applications. Elsevier.

Kofman, W., Herique, A., Barbin, Y., Barriot, J.-P., Ciarletti, V., Clifford, S., Edenhofer, P., Elachi, C., Eyraud, C., Goutail, J.-P., Heggy, E., Jorda, L., Lasue, J., Levasseur-Regourd, A.-C., Nielsen, E., Pasquero, P., Preusker, F., Puget, P., Plettemeier, D., Rogez, Y., Sierks, H., Statz, C., Svedhem, H., Williams, I., Zine, S., Van Zyl, J., 2015. Properties of the 67P/Churyumov-Gerasimenko interior revealed by CONSERT radar. Science 349 (6247).

Kosloff, D.D., Baysal, E., 1983. Migration with the full acoustic wave equation. Geophysics 48 (06), 677–687.

Lailly, P., 1983. The seismic inverse problem as a sequence of before stack migrations. In: Proceedings of the Conference on Inverse Scattering, Theory and Application, pp. 206–220.

McMechan, G.A., 1983. Migration by extrapolation of time-dependent boundary values. Geophys. Prosp. 31 (03), 413–420.

Miller, R.D., Bradford, J.H. (Eds.), 2010. Advances in Near-Surface Seismology and Ground-Penetrating Radar. Society of Exploration Geophysicists.

Morbidelli, A., Rickman, H., 2015. Comets as collisional fragments of a primordial planetesimal disk. Astron. Astrophys. 583, A43.

Nemeth, T., Wu, C., Schuster, G., 1999. Least-squares migration of incomplete reflection data. Geophysics, 208–221.

Nolet, G., 2008. A Breviary of Seismic Tomography: Imaging the Interior of the Earth and Sun. Cambridge University Press.

Prati, C., Rocca, F., Guarnieri, A.M., Damonti, E., 1990. Seismic migration for SAR focusing: interferometrical applications. IEEE Trans. Geosci. Remote Sens. 28 (4).

Reynolds, J.M., 1997. An Introduction to Applied and Environmental Geophysics, second ed. Wiley.

Richards, M., 2014. Fundamentals of Radar Signal Processing. McGraw-Hill.

Rocca, F., Cafforio, C., Prati, C., 1989. Synthetic Aperture Radar: a new application for wave equation techniques. Geophys. Prospect. 37, 809–830.

Safaeinili, A., Gulkis, S., Hofstadter, M., Jordan, R., 2002. Probing the interior of asteroids and comets using radio reflection tomography. Meteor. Planet. Sci. 37, 1953–1963.

Sava, P.C., Asphaug, E., 2018. 3D radar wavefield tomography of comet interiors. Adv. Space Res. 61, 2198–2213.

Sava, P.C., Ittharat, D., Grimm, R., Stillman, D., 2015. Radio reflection imaging of asteroid and comet interiors I: acquisition and imaging theory. Adv. Space Res. 55, 2149–2165.

Scheeres, D., Marzari, F., Tomasella, L., Vanzani, V., 1998. ROSETTA mission: satellite orbits around a cometary nucleus. Planet. Space Sci. 46 (6), 649–671.

Sierks, H., Barbieri, C., Lamy, P.L., Rodrigo, R., Koschny, D., Rickman, H., Keller, H.U., Agarwal, J., A'Hearn, M.F., Angrilli, F., Auger, A.-T., Barucci, M.A., Bertaux, J.-L., Bertini, I., Besse, S., Bodewits, D., Capanna, C., Cremonese, G., Da Deppo, V., Davidsson, B., Debei, S., De Cecco, M., Ferri, F., Fornasier, S., Fulle, M., Gaskell, R., Giacomini, L., Groussin, O., Gutierrez-Marques, P., Gutiérrez, P.J., Güttler, C., Hoekzema, N., Hviid, S.F., Ip, W.-H., Jorda, L., Knollenberg, J., Kovacs, G., Kramm, J.R., Kührt, E., Küppers, M., La Forgia, F., Lara, L.M., Lazzarin, M., Leyrat, C., Lopez Moreno, J. J., Magrin, S., Marchi, S., Marzari, F., Massironi, M., Michalik, H., Moissl, R., Mottola, S., Naletto, G., Oklay, N., Pajola, M., Pertile, M., Preusker, F., Sabau, L., Scholten, F., Snodgrass, C., Thomas, N., Tubiana, C., Vincent, J.-B., Wenzel, K.-P., Zaccariotto, M., Pätzold, M., 2015. On the nucleus structure and activity of comet 67P/Churyumov-Gerasimenko. Science 347 (6220).

Stillman, D.E., Grimm, R.E., Dec, S.F., 2010. Low-frequency electrical properties of ice–silicate mixtures. J. Phys. Chem. B 114 (18), 6065–6073.

Thomas, P., AH´earn, M., Belton, M., Brownlee, D., Carcich, B., Hermalyn, B., Klaasen, K., Sackett, S., Schultz, P., Veverka, J., Bhaskaran, S., Bodewits, D., Chesley, S., Clark, B., Farnham, T., Groussin, O., Harris, A., Kissel, J., Li, J.-Y., Meech, K., Melosh, J.,

Quick, A., Richardson, J., Sunshine, J., Wellnitz, D., 2013. The nucleus of comet 9P/Tempel 1: shape and geology from two flybys. Icarus 222 (2), 453–466, Stardust/EPOXI.

Veverka, J., Klaasen, K., A'Hearn, M., Belton, M., Brownlee, D., Chesley, S., Clark, B., Economou, T., Farquhar, R., Green, S., Groussin, O., Harris, A., Kissel, J., Li, J.-Y., Meech, K., Melosh, J., Richardson, J., Schultz, P., Silen, J., Sunshine, J., Thomas, P., Bhaskaran, S., Bodewits, D., Carcich, B., Cheuvront, A., Farnham, T., Sackett, S., Wellnitz, D., Wolf, A., 2013. Return to comet Tempel 1: overview of Stardust-NExT results. Icarus 222 (2), 424–435.